Analytic Solutions to Determine Critical Magnetic Fields for Thermoelectric Magnetohydrodynamics in Alloy Solidification

A. Kao

Centre of Numerical Modelling & Process Analysis,
University of Greenwich,
Old Royal Naval College,
Park Row, London SE10 9LS, UK

Keywords: Critical Magnetic Fields, Thermoelectric Magnetohydrodynamics, Dendritic Solidification

Abstract

During alloy solidification, it has been observed that the morphology of microstructures can be altered by applying an external DC magnetic field. This structural change can be attributed to solutal convective transport introduced by Thermoelectric Magnetohydrodynamics (TEMHD) which drives fluid motion within the inter-dendritic region. Complex numerical models with grid resolutions on the microscopic scale have been constructed to solve the equations governing TEMHD. To complement these computationally intensive numerical models, analytic solutions were sought. Specifically, the analytic solutions presented herein are asymptotic solutions derived for TEMHD under low and high magnetic field intensities. Combination of these asymptotic solutions leads to simple formulae for estimating critical magnetic fields which can be readily evaluated in terms of characteristic lengths of materials that have been identified in experiments as key parameters of critical fields. Indeed, the critical magnetic fields predicted with the asymptotic solutions exhibit magnitudes consistent with those applied in current ongoing experiments where significant changes in microstructure have been observed. The capability to predict accurate results indicates that the analytic solutions described herein are valuable precusors not only for detailed numerical simulations but also for experimental design to study critical magnetic fields in alloy solidification.

Introduction

The ability to control microstructural evolution of solidifying alloys is of fundamental importance for modifying and tailoring material properties. Thermal gradients and stirring are examples of controls currently used in industry for manufacturing alloys. The introduction of magnetic fields into the solidifying process offers another control for alloy production. To increase knowledge of these controlling mechanisms, numerical models have been constructed (for example, Kao *et al.* [1–4]) to solve the equations governing the complex physical processes of solidification under the influence of magnetic fields. These equations describe mass, energy and momentum transport in the vicinity of the solid-liquid interface coupled with the thermoelectrically-induced Lorentz forces. In this paper, the author presents another approach for solving these equations with the objective of deriving analytic solutions that can be readily evaluated to provide useful previews of results prior to initiating the time-consuming but necessary numerical simulations for parametric studies on solidification under the influence of magnetic fields.

Experiments [5, 6] and numerical models [7, 8] have shown that forced convection can have a significant impact on the microstructure evolution with effects such as preferential growth, grain refinement and macrosegregation all being observed and predicted. Typically, fluid flow is introduced through traditional electromagnetic stirring using an AC field. Any DC field present will act as a damping mechanism. Under certain thermal conditions, natural and inherent thermoelectric currents can be generated as a result of the Seebeck effect. When these currents interact with an external DC magnetic field, a Lorentz force is formed which becomes the driver of fluid motion. This effect, known as Thermoelectric Magnetohydrodynamics (TEMHD), was first detailed by Shercliff who demonstrated that processes with large thermal gradients and a significant thermoelectric power, could attain relatively high fluid velocities [9]. Shercliff applied the TEMHD theory to several phenomena related to nuclear fusion reactors [10, 11] and showed, as an example, that under a moderate magnetic field strength, velocities of $O(10\text{cm/s})$ in liquid Lithium could be achieved. Indeed recent experiments [12] support Shercliff's theoretical work on TEMHD.

TEMHD has gained recognition as a potential cost-effective, low-energy, stirring mechanism. For example, experiments with a moderate thermal gradient of 2.8K/cm and a thermoelectric power of 20μK/V have demonstrated that a rare earth Neodymium magnet alone would be sufficient to achieve velocities of O(33mm/s) in a conducting fluid without the need for electromagnets [13, 14]. Furthermore, TEMHD has been shown to impact natural convection [15].

The aforementioned references all investigated TEMHD on the macroscopic scale. However, variations in surface temperature, such as the large thermal gradients created during directional solidification, can produce conditions for thermoelectric currents to form on the micro-meso scale. Accordingly, the analytic model described in this paper and the numerical model referenced for comparison of results both address TEMHD in alloy solidification on the micro-meso scale.

The use of TEMHD for controlling solidification was first proposed and investigated in the 1990s [16–18]. Those experiments showed that the application of an external DC magnetic field to a solidifying alloy had pronounced effects on the crystalline structure. Also, the magnitude of the changes had a material dependency which could be attributed to the variation in thermoelectric power of the various alloys examined. More recently, microstructural changes have been observed over a wide range of magnetic field intensities from low-moderate (O(1T)) field strengths [19–22] to higher (O(10T)) strengths [23–25]. Furthermore, direct *in situ* observations of solidification under a relatively low magnetic field have shown indications of TEMHD flow at the meso scale [26].

Experiments conducted to explore the impact of magnetic field intensity on microstructures have also identified the presence of a critical magnetic field which occurs when the dominant opposing force changes from viscous damping to electromagnetic damping. During this transition, the conditions for maximum flow velocity are produced resulting in the largest microstructural change [19]. The analytic solutions for TEMHD described in this paper would readily reveal the functional dependency and the physical parameters for determining the critical magnetic field. The significance of these parameters is of particular interest for developing the capability to predict the outcome of microstructural modifications which in turn will allow macroscopic material properties to be tailored by selective design of the applied magnetic field.

Thermoelectric magnetohydrodynamics

Thermoelectricity is essentially the conversion of thermal energy into electrical energy, the fundamentals of which are detailed in semi-conductor physics. This section summarises the basic equations governing TEMHD and the assumptions made to simplify these equations in order to derive analytic solutions.

Governing equations

In solidification, there are two necessary conditions for thermoelectric currents to exist. The first is a temperature variation on the liquid-solid interface and the second is a difference in thermoelectric power ΔS across the liquid-solid interface. In directional solidification, the former condition is immediately satisfied by an externally imposed thermal gradient. For the latter condition, the alloy components can be chosen such that a significant ΔS exists between the solid phase and the high concentration of locally ejected solute at the interface.

The Seebeck effect can be quantified by generalising Ohm's law with the inclusion of a thermoelectric term $S\nabla T$

$$\frac{\mathbf{j}}{\sigma} = \mathbf{E} - S\nabla T + \mathbf{u} \times \mathbf{B} \tag{1}$$

where $\mathbf{j}$ is the current density, σ is the electrical conductivity, $\mathbf{E}$ is the electric field, S is the Seebeck coefficient, $\mathbf{u}$ is the flow velocity and $\mathbf{B}$ is the magnetic field. The thermoelectric potential Ψ_T is defined as $\Psi_T(T) = \int S dT$ which simply becomes $\Psi_T = ST$ for constant S. In terms of potentials, (1) can be expressed as

$$\frac{\mathbf{j}}{\sigma} = -\nabla(\Psi_E + \Psi_T) + \mathbf{u} \times \mathbf{B} = -\nabla\Psi + \mathbf{u} \times \mathbf{B}. \tag{2}$$

where Ψ is the combined potential of Ψ_T and the electric potential Ψ_E. Taking the divergence of (2) together with continuity of charge $\nabla \cdot \mathbf{j} = 0$ reduces (2) to Poisson's equation

$$\nabla^2\Psi = \nabla \cdot \mathbf{u} \times \mathbf{B}. \tag{3}$$

At the liquid-solid interface, the driving e.m.f is

$$\Delta\Psi = \oint \frac{\mathbf{j}}{\sigma} \cdot dl. \tag{4}$$

Integrating around the interface between two loca-

tions with temperatures T_1 and T_2 gives

$$\begin{aligned}\Delta\Psi &= \Psi_E^i - \int_{T_2}^{T_1} S_l \nabla T \cdot dl + (\mathbf{u}\times\mathbf{B})_{||} \\ &\quad - \Psi_E^i + \int_{T_2}^{T_1} S_s \nabla T \cdot dl \\ &= \int_{T_2}^{T_1} (S_l - S_s)\, dT = \int_{T_2}^{T_1} \Delta S dT + (\mathbf{u}\times\mathbf{B})_{||}\,. \quad (5)\end{aligned}$$

where $(\mathbf{u}\times\mathbf{B})_{||}$ is parallel to the interface and the subscripts l and s represent liquid and solid respectively. With constant S assigned to both solid and liquid, the potential difference simplifies to

$$\Delta\Psi = \Delta S T + (\mathbf{u}\times\mathbf{B})_{||} \quad (6)$$

In the presence of an external magnetic field, these currents will interact to give a Lorentz force for fluid motion. For time-invariant magnetic fields, this type of MHD flow can be described by the classical Navier-Stokes equation

$$\rho\left(\frac{\partial\mathbf{u}}{\partial t} + \mathbf{u}\cdot\nabla\mathbf{u}\right) = -\nabla p + \mu\nabla^2\mathbf{u} + \mathbf{j}\times\mathbf{B} \quad (7)$$

where the last term on the right hand side represents the Lorentz force. Finally, continuity for incompressible flow

$$\nabla\cdot\mathbf{u} = 0 \quad (8)$$

completes the set of equations governing TEMHD.

Assumptions

The key result presented in this paper is a set of analytic solutions describing dendritic growth under the influence of an applied magnetic field in directional solidification. Asymptotic solutions are derived applicable for low magnetic fields denoted by $\mathbf{B_0}$, for $\mathbf{B}\to 0$, as well as high magnetic fields denoted by $\mathbf{B}_\infty$, for $\mathbf{B}\to\infty$. For clarity, this section summarises the assumptions made in order to derive the analytic solutions.

The first assumption made is a low Seebeck power $\Delta S \sim 0$ which, irrespective of the magnitude the of magnetic field, will produce a low driving force, hence low velocities implying low Reynolds numbers Re. Note that a low Re is also consistent with the typical dimensions of microstructures. The second assumption made is that the time-scale for transport of heat and mass is much smaller than the acceleration time of the fluid flow which, for advective transport, is automatically satisfied by the low Re. For diffusion, the second assumption becomes valid when the crystals are in a quasi thermodynamic equilibrium state. Based on these two assumptions, the temporal and convective acceleration terms in the Navier-Stokes equation (7) can be removed to give the steady-state equation

$$-\nabla p + \mu\nabla^2\mathbf{u} + \mathbf{j}\times\mathbf{B} = 0. \quad (9)$$

Let

$$\mathbf{j}\times\mathbf{B} = \mathbf{J}\times\mathbf{B} + \sigma\mathbf{u}\times\mathbf{B}\times\mathbf{B} \quad (10)$$

where the Lorentz force is expressed as the sum of the driving thermoelectric force and the electromagnetic damping force. For a low magnetic field, $\mathbf{B}\to 0$, thus $\mathbf{u}\times\mathbf{B}\to 0$ and for a high magnetic field, it can be assumed that

$$\left|\mu\nabla^2\mathbf{u}\right| << |\mathbf{J}\times\mathbf{B}| \sim |\sigma\mathbf{u}\times\mathbf{B}\times\mathbf{B}| \quad (11)$$

giving

$$|\mathbf{u}| \propto \frac{\Delta S}{|\mathbf{B}|} \quad (12)$$

which leads to the result

$$|\mathbf{u}\times\mathbf{B}| \propto \Delta S \sim 0. \quad (13)$$

The simplifications based on the above assumptions for both low and high magnetic fields show that the term $\mathbf{u}\times\mathbf{B}$ in (6) can be removed giving

$$\Delta\Psi = \Delta S T. \quad (14)$$

For a low magnetic field $\mathbf{B_0}$, the electromagnetic damping force vanishes while the viscous damping force dominates. (9) then becomes

$$-\nabla p + \mu\nabla^2\mathbf{u} + \mathbf{J}\times\mathbf{B_0} = 0. \quad (15)$$

For a high magnetic field $\mathbf{B}_\infty$, the electromagnetic damping term

$$\mathbf{u}\times\mathbf{B}_\infty\times\mathbf{B}_\infty \propto S\nabla T\times\mathbf{B}_\infty$$

is significant but viscous damping is negligible. In this case, (9) becomes

$$-\nabla p + \mathbf{J}\times\mathbf{B}_\infty + \sigma\mathbf{u}\times\mathbf{B}_\infty\times\mathbf{B}_\infty = 0. \quad (16)$$

In the subsequent analysis for analytic solutions, reference to low magnetic fields $\mathbf{B_0}$ implies significant viscous damping with negligible electromagnetic damping. Likewise, high magnetic fields $\mathbf{B}_\infty$ are synonymous with significant electromagnetic damping and negligible viscous damping.

Steady State Analysis Under Directional Solidification

During directional solidification, the external thermal conditions are controlled by two furnaces operating at different temperatures which create a thermal gradient along the direction of solidification $\hat{z}$. The applied temperature gradient causes dendritic growth to take on a columnar structure. For the purpose of analytic derivations, it can be assumed that the external thermal conditions will dominate over any localised surface energy effects and that heat loss normal to the applied thermal gradient will be negligible. Under these conditions, the temperature gradient will be constant throughout the system and the potential difference at the solid-liquid interface becomes

$$\Delta\Psi = \Delta S \frac{dT}{dz} z. \tag{17}$$

Figure 1 shows results from a numerical simulation depicting an example of the typical columnar structure of dendritic growth during directional solidification. The accompanying solution for the thermoelectric current **J**, also shown in this figure, illustrates that current passes inside the dendrite before emanating near the tip, then through the liquid and continues across the lower boundary at the base of the dendrite.

The main objective of this paper is to determine critical magnetic fields for transverse and parallel field orientations in directional solidification. The common form for the critical magnetic field, as derived from MHD duct flow, is given by

$$B_c = \frac{1}{W}\left(\frac{\mu}{\sigma}\right)^{\frac{1}{2}} \tag{18}$$

where the characteristic length W is half of the duct width. The simplistic form of (18) comprising only a single characteristic length lacks the definition for accurate estimation of critical fields as there are many lengths scales in solidification ranging over several orders of magnitude from the radius of a dendrite tip $W \sim 10^{-6}$m to the length of the material itself $W > 10^{-3}$m. This paper addresses the variety of length scales by determining analytic solutions that include characteristic lengths of materials which are known from experiments to be key parameters of critical magnetic fields. Specifically, these characteristic lengths are the primary tip radius r_0, half of the primary arm spacing W_p, half of the secondary arm radius W_r and half of the grain spacing W_s.

The analytic solutions presented in this paper provide formulae for critical magnetic fields based on two definitions. The first denoted by B_c defines the magnetic field that produces the maximum velocity and the second denoted by B_{cfr} defines the magnetic field that maximises the flow rate. The selection of definition for critical fields is application dependent. For example, the former B_c may be easier to detect experimentally for validation while the latter B_{cfr} is more closely linked to convective transport and therefore directly related to morphological changes. The general formulae for critical magnetic fields derived from the analytic solutions are applicable for a wide range of alloys. As an illustration for industrial applications, the numerical and analytic results described in the following analyses have been scaled to represent an aluminium-based alloy with material properties of $\mu = 1.3 \times 10^{-3}$Pas and $\sigma = 3.78 \times 10^{7}$S/m.

Transverse magnetic field

This section details the derivation of analytic solutions for directional solidification in the presence of an external transverse magnetic field. Near the base of the crystal, as illustrated in figure 1, **J** will have a dominant component J_z. For the purpose of deriving analytic solutions, the other vector components of **J** can be ignored based on the following analogue.

Consider an infinite array of infinitely long uniform wires aligned parallel to the thermal gradient with alternating Seebeck coefficients. Because of the constant external thermal gradient, the thermoelectric field $S\nabla T$ within each wire will remain constant and with no variations in the geometry of the wires, the electric field $-\nabla\Psi_E$ will also be constant. Consequently, the current density within each wire will be constant but in opposite directions. This analogue represents a cross-section through the dendritic array with alternating wires representing solid and liquid. Physically, the analogue can be applied within the inter-dendritic region away from the tips where the dendrites are closely packed. In this region, the resulting force under a B_y magnetic field will only have a single component in the $\hat{x}$ direction.

Figure 2 shows the results of a numerical simulation depicting the flow pattern around dendrites under a moderate magnetic field. These results show inter-dendritic flow passing between the crystals with twin circulations forming around each tip. Assuming that these twin vortices do not influence flow at the base of the dendrite, this infinite array of dendrites can be viewed as a series of alternate expanding and contracting ducts. Figure 3 shows a schematic cross-section of these ducts. For brevity, the nar-

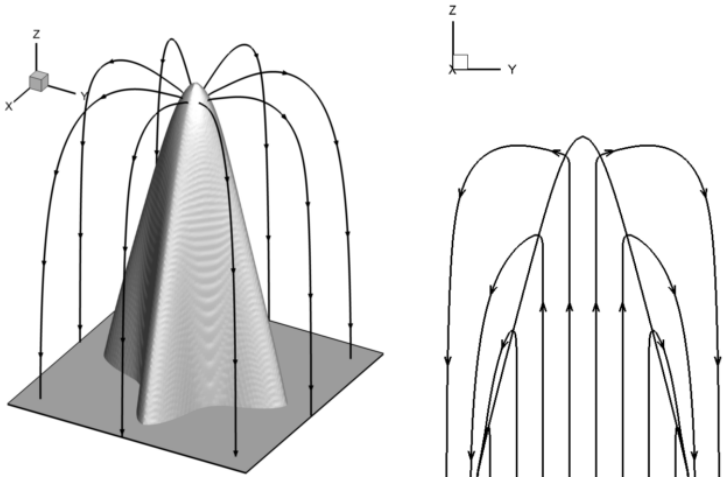

Figure 1: **J** for directional solidification

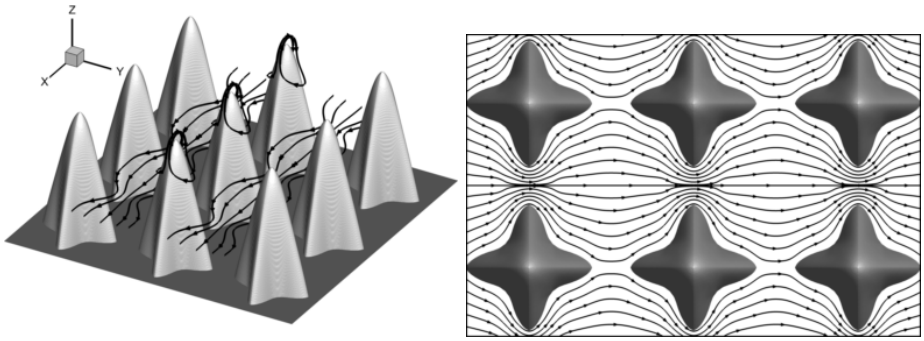

Figure 2: Example representation of the flow near the base of the crystal under a transverse field.

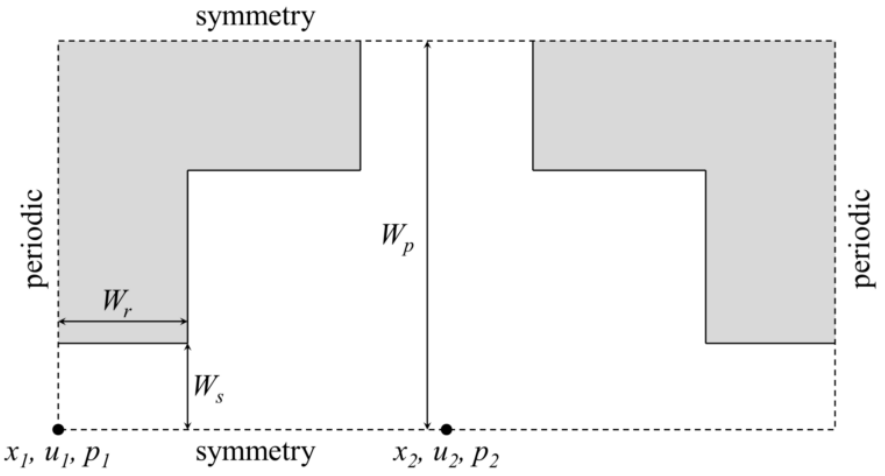

Figure 3: Representation of infinite series of pipe expansion and contractions.

rower region between two secondary branches of different dendrites will be referred to as the secondary duct and the wider region between the primary arms, the primary duct. In order to derive analytic solutions for flow within both the primary and secondary ducts, the flow at the centre of each duct is assumed to be fully developed. Also, laminar flow within the ducts is implied as a result of low *Re*. The various lengths and nomenclature used in the following analysis are also shown in figure 3 where u_1, p_1 are the velocity and pressure in the centre of the secondary duct x_1 and u_2, p_2 are the velocity and pressure in the centre of the primary duct x_2.

For a low magnetic field $\mathbf{B_0}$, the Navier-Stokes equation can be expressed as

$$-J_z B_0 + \mu \frac{\partial^2 u}{\partial y^2} - \frac{\partial p}{\partial x} = 0 \tag{19}$$

with boundary conditions for the secondary duct

$$u_1|_{y=W_s} = 0, \tag{20}$$

$$\left.\frac{\partial u_1}{\partial y}\right|_{y=0} = 0, \tag{21}$$

$$\left.\frac{\partial}{\partial y}\frac{\partial p_1}{\partial x}\right|_{y=0} = 0 \tag{22}$$

and for the primary duct

$$u_2|_{y=W_p} = u_w, \tag{23}$$

$$\left.\frac{\partial u_2}{\partial y}\right|_{y=0} = 0, \tag{24}$$

$$\left.\frac{\partial u_2}{\partial y}\right|_{y=W_p} = 0, \tag{25}$$

$$\left.\frac{\partial}{\partial y}\frac{\partial p_2}{\partial x}\right|_{y=0} = 0, \tag{26}$$

$$\left.\frac{\partial}{\partial y}\frac{\partial p_2}{\partial x}\right|_{y=W_p} = 0 \tag{27}$$

where u_w is the velocity at the primary duct boundaries. For each duct, the lowest order solutions for the velocity and pressure gradient that satisfy the number of critcal points imposed by the boundary conditions can be expressed as

$$u_1 = A_0 + A_2 y^2, \tag{28}$$

$$\frac{\partial p_1}{\partial x} = C_0, \tag{29}$$

$$u_2 = D_0 + D_2 y^2 + D_4 y^4 + D_6 y^6, \tag{30}$$

$$\frac{\partial p_2}{\partial x} = E_0 + E_2 y^2 + E_4 y^4 \tag{31}$$

where flow in the secondary duct is characterised by Pouseuille flow. By applying mass conservation together with an assumed linear pressure trend at x_1 and x_2, the coefficients in the above equations can be solved analytically. Full derivation of all the coefficients is described in the Appendix. The salient ones, which represent fluid flow along the centre of the ducts, are shown below.

$$A_0 = \frac{1}{2\mu W_0}\left(-16 J_z B_0 W_p^3 + 147\mu u_w \left(W_p - W_r\right)\right) W_p W_s^2, \tag{32}$$

$$C_0 = \frac{1}{W_0}\left(J_z B_0 \left(16W_p^3 - 49W_s^3\right) - 147\mu u_w W_p\right)\left(W_p - W_r\right), \tag{33}$$

$$D_0 = -\frac{1}{2\mu W_0}\left(21 J_z B_0 W_s^3 W_p^3 + \mu u_w \left(31W_p^3 W_r - 98W_p W_s^3 + 98W_r W_s^3\right)\right), \tag{34}$$

$$E_0 = \frac{1}{W_0}\left(J_z B_0 \left(-16W_p^3 + 49W_s^3\right) + 147\mu u_w W_p\right) W_r, \tag{35}$$

$$W_0 = 49W_s^3\left(W_p - W_r\right) + 16W_p^3 W_r. \tag{36}$$

The above results for low magnetic fields show that the velocity increases with increasing B_y. In general, the velocity at the primary duct boundaries u_w is unknown but $|u_w| << D_0$ is a reasonable approximation. Therefore, in the subsequent analysis, $u_w = 0$ has been assumed.

For a high magnetic field $\mathbf{B}_\infty$, as characterised by a high Hartmann number, the viscous boundary layer becomes thin resulting in negligible viscous damping along the duct centres. Under these conditions, the Navier-Stokes equation simplifies to

$$-J_z B_\infty - \sigma u B_\infty^2 - \frac{\partial p}{\partial x} = 0 \tag{37}$$

which can be solved as

$$u_1 = -\frac{J_z W_p^2}{\sigma B_\infty W_\infty}, \tag{38}$$

$$u_2 = -\frac{J_z W_p W_s}{\sigma B_\infty W_\infty}, \tag{39}$$

$$\frac{\partial p_1}{\partial x} = \frac{J_z B_\infty \left(W_r - W_p\right)\left(W_p - W_s\right)}{W_\infty}, \tag{40}$$

$$\frac{\partial p_2}{\partial x} = -\frac{J_z B_\infty W_r \left(W_p - W_s\right)}{W_\infty}, \tag{41}$$

$$W_\infty = W_r\left(W_p - W_s\right) + W_p W_s. \tag{42}$$

The above results for high magnetic fields show that the velocity decreases with increasing B_y.

In both ducts, the low field solution represents viscous damped flow while the high field solution represents Hartmann flow. For comparison between the analytic and numerical methods, a section at the base of the dendrite was selected with the following lengths $W_p = 18.0\mu$m, $W_s = 4.6\mu$m and $W_r = 3.4\mu$m. The relatively small primary arm spacing of 36.0μm between each dendrite was chosen so that a sufficiently fine 3-dimensional grid containing some 12 million cells discretised with constant dimensions of 0.25μm would cover the entire domain for numerical computations.

Figure 4 shows the results from the analytic and numerical solutions for a case with a low magnetic field strength of $B_y = 10^{-7}$T. Comparison of results in this figure indicates a more accurate match for the primary duct than for the secondary duct. The larger discrepancy of the latter can be attributed to the following effects. Firstly, as might be expected of the relatively short duct length, the numerical flow profile is not parabolic nor fully developed. Secondly, a pressure gradient along the direction of solidification will be created by the tapering geometry of the secondary duct. This geometric effect produces additional perturbations in the conservation equations for momentum and mass which were excluded in the derivation of the analytic solutions. Nevertheless, the analytic solution for the secondary duct still matches the numerical results near the duct boundaries. Figure 5 shows the analytic and numerical results for a case with a high magnetic field strength of $B_y = 10$T. Notice that Hartmann flow is clearly evident in both ducts with the analytic solution representing idealised Hartmann flow. Figure 6 shows pressure variations within the primary and secondary ducts for the cases with low and high magnetic field strengths. The periodic pressure condition from (98), also shown in this figure, is in excellent agreement with the numerical solutions particularly at x_1 and x_2.

The analytic solutions for the cases of low and high magnetic fields where respectively electromagnetic damping and viscous damping have been neglected show that as B_y increases, the low magnetic field velocity increases linearly with B_y while the high magnetic field velocity decreases as the inverse of B_y. Combination of these two asymptotic solutions will form the envelope within which the numerical solution, which includes electromagnetic and viscous damping, would lie. This envelope indicates the presence of a critical magnetic field B_c where transition from viscous damped to Hartmann flow occurs within the secondary and primary ducts. This critical magnetic field can be defined as the field strength that gives a maximum velocity which occurs when

$$\left.\frac{\partial u}{\partial B}\right|_{B_y=B_c} = 0. \tag{43}$$

For each duct, the critical magnetic field can be determined by equating the low and high magnetic field solutions at x_1 and x_2 and solving for B_y. The following are the solutions for the critical magnetic fields in the secondary and primary ducts.

$$B_c|_{x_1} = \frac{1}{W_p W_s}\left(\frac{\mu W_0}{8\sigma W_\infty}\right)^{\frac{1}{2}}, \tag{44}$$

$$B_c|_{x_2} = \frac{1}{W_p W_s}\left(\frac{2\mu W_0}{21\sigma W_\infty}\right)^{\frac{1}{2}} \tag{45}$$

where

$$B_c|_{x_1} > B_c|_{x_2}\,. \tag{46}$$

Figure 7 shows the numerical results for the velocity at the centre of both ducts over the range of magnetic fields simulated. Also shown in this figure are the low and high field asymptotic solutions, the intersection of which determines the critical fields as given in (44) and (45). Note that the strengths of the critical field predicted analytically are in reasonable agreement with the numerical results.

For convective transport, the critical magnetic field B_{cfr} creates the highest flow rate in both ducts. There are four flow rates, two for each duct with low and high magnetic fields. Applying continuity,

$$\int_{y=0}^{y=W_s} u_1(B_0)dy = \int_{y=0}^{y=W_p} u_2(B_0)dy$$
$$= \int_{y=0}^{y=W_s} u_1(B_\infty)dy = \int_{y=0}^{y=W_p} u_2(B_\infty)dy, \tag{47}$$

from which any combination of low and high field solutions can be used to calculate the critical magnetic field B_{cfr}. The flow rates for the low field solution in the secondary duct and the high field solution in the primary duct are given respectively by

$$u_{1fr} = \int_{y=0}^{y=W_s} u_1 dy = -\frac{16}{3}\frac{J_z B_0 W_p^4 W_s^3}{\mu W_0}$$
$$= F_0 B_0, \tag{48}$$

$$u_{2fr} = \int_{y=0}^{y=W_p} u_2 dy = \frac{-J_z W_p^2 W_s}{\sigma B_\infty W_\infty} = \frac{F_\infty}{B_\infty}. \tag{49}$$

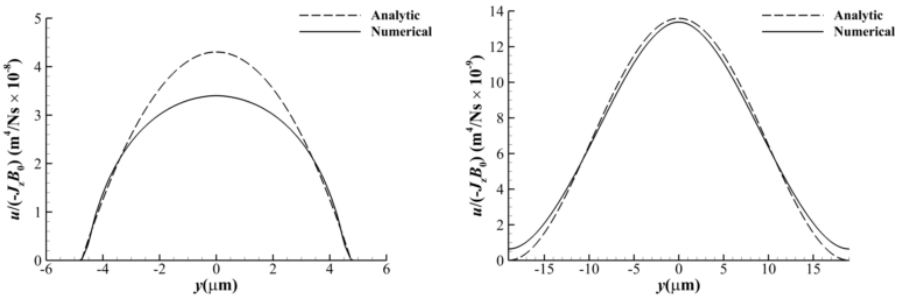

Figure 4: x-velocity profile under a low magnetic field. Left: Secondary duct. Right: Primary duct.

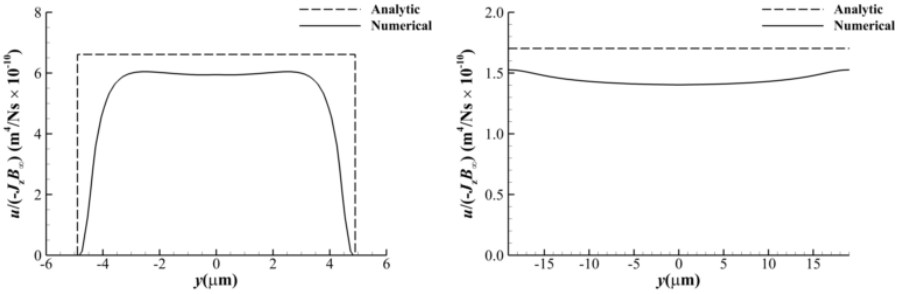

Figure 5: x-velocity profile under a high magnetic field. Left: Secondary duct. Right: Primary duct.

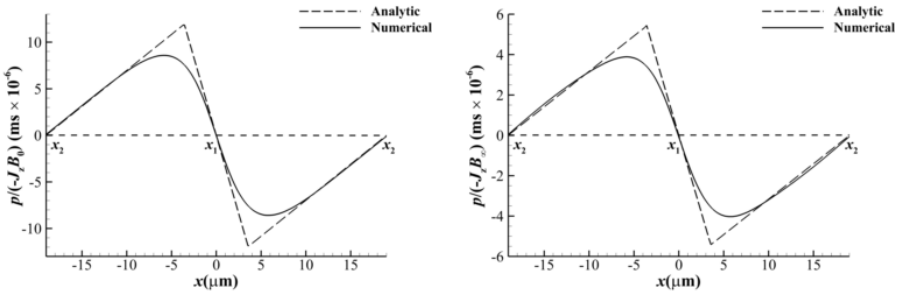

Figure 6: Pressure along the centre of the two ducts. Left: Low magnetic field. Right: High magnetic field.

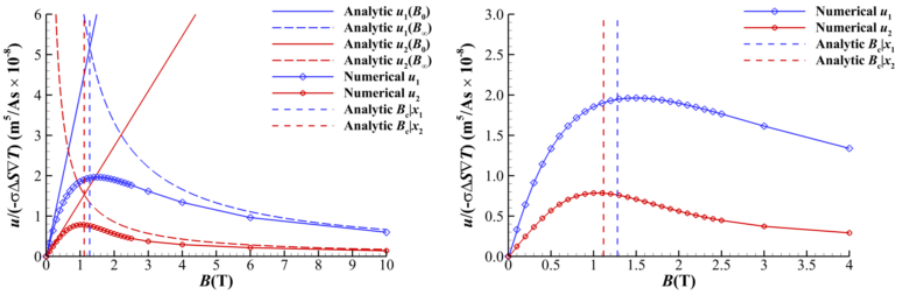

Figure 7: Comparison of asymptotic solutions for u_1 and u_2 against numerical simulations. The right figure is focused around the predicted critical magnetic fields

Equating (48) to (49) and setting $B_{cfr} = B_0 = B_\infty$, the critical field can be solved as

$$B_{cfr} = \frac{1}{W_p W_s}\left(\frac{3\mu W_0}{16\sigma W_\infty}\right)^{\frac{1}{2}}. \tag{50}$$

Figure 8 shows the resulting asymptotic solutions for low and high magnetic fields together with the critical magnetic field where these solutions intersect. Note the successful match of the critical magnetic field B_{cfr} to the numerical results.

The simple forms of the asymptotic solutions for the flow rates (48) and (49) suggest that the low and high field solutions can be linked into a single analytic function $u_{fr}(B)$ for all magnetic field strengths B. Indeed, the following linkage of the low and high field asymptotic solutions

$$u_{fr} = (\frac{1}{F_0 B} + \frac{B}{F_\infty})^{-1}, \tag{51}$$

also shown in figure 8, improves the match of the analytic solution to the numerical solution for u_{fr} by a factor of 2 when compared to using (48) and (49) in isolation. More importantly, the maximum of (51), which defines the critical magnetic field, occurs at the same value as the intersection of the low and high field asymptotic solutions given by (50)

The above derivation of (50) shows that the critical magnetic field depends on several length scales. Dimensional analysis with

$$W_0 \to W_{Ha}^4, \tag{52}$$

$$W_\infty \to W_{Ha}^2, \tag{53}$$

$$W_p \sim W_s \sim W_r \to W_{Ha} \tag{54}$$

simplifies (50) to

$$B_c|_{x_1,x_2,fr} = \frac{O\,(1)}{W_{Ha}}\left(\frac{\mu}{\sigma}\right)^{\frac{1}{2}} \tag{55}$$

where W_{Ha} represents a modified Hartmann layer or characteristic length analogous to W in (18). For application in conventional castings where a uniform temperature gradient can be generated as molten alloy is cooled at one end of a cast, the early stages of solidification can be described by (55) with $W_s \sim W_p >> W_r$ which gives

$$B_c|_{x_1,x_2,fr} \propto \frac{1}{W_p}\left(\frac{\mu}{\sigma}\right)^{\frac{1}{2}}. \tag{56}$$

Note that in (56), the critical magnetic fields depends on the primary arm spacing W_p but during later stages of solidification, when $W_s \sim W_r << W_p$, the critical magnetic fields become

$$B_c|_{x_1,x_2,fr} \propto \frac{1}{W_s}\left(\frac{\mu}{\sigma}\right)^{\frac{1}{2}} \tag{57}$$

and depend only on the grain spacing W_s.

The effects of TEMHD for low magnetic fields will be greatest close to the tips but for high magnetic fields, the largest influence will occur deep within the inter-dendritic network. For practical applications, the analytic solution can be useful for determining the required operational strength of the applied magnetic field by simply estimating the characteristic length scales of the regions targeted for material changes. As an illustration of the application of the analytic solution, evaluating (50) with typical material properties and dimensions of $\mu = 10^{-3}$Pas, $\sigma = 10^7$S/m, $W_p = 200\mu$m, $W_r = 5\mu$m and $10 < W_s > 100\mu$m gives a B_{cfr} ranging from 0.15 - 1.02T. In the limit when grain boundaries become very thin, for example $W_s < 1\mu$m, the required critical field could exceed 10T.

Parallel magnetic field

Consider the same system as described in the previous section but now the external magnetic field is aligned to the direction of dendritic growth. At the base of the crystal, **J** will predominantly be parallel to the direction of the magnetic field, hence the resulting Lorentz force will be neglible. However, at the tip of the crystal, **J** will have components tangential to the magnetic field with a significant Lorentz force generated. In the following analysis, the governing equations are re-cast in cylindrical polar coordinates (r, θ, z) and the derivation of analytic solutions is conducted in the plane that intersects the dendrite tip radius r_0 where the Lorentz force and velocity are significant. At this location, the system is approximately axisymmetric, hence

$$\frac{\partial f}{\partial \theta} = 0 \tag{58}$$

where f represents all spatially dependent variables. For current density, this approximation gives

$$J_\theta = \frac{1}{r}\frac{\partial \Psi}{\partial \theta} = 0. \tag{59}$$

Physically, J_r will decrease away from the dendrite interface or with increasing r. Examination of numerical simulation results describing this behaviour

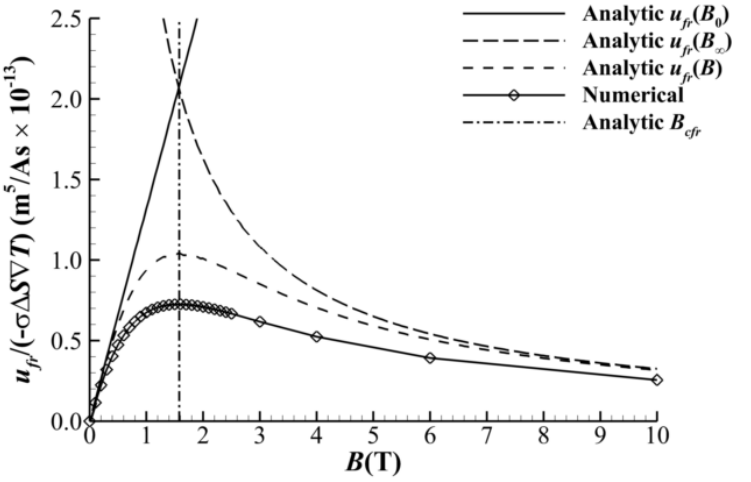

Figure 8: Comparison of asymptotic solutions for u_{fr} against numerical simulations.

concluded that J_r can be approximated by a power law in the form of

$$J_r = J_0 \left(r^{n-2} - W_p^{n-2} \right) \tag{60}$$

such that J_r decays to zero at the periodic boundary $r = W_p$ with continuity of $\mathbf{J}$ preserved. The coefficient J_0 in (60) is proportional to the thermoelectric field and the exponent n determines the decay of J_r as $r \to W_p$. n is predominantly dependent on the dendritic morphology and for most practical application, lies between 1 and 0. A value of unity represents the analogous solution for an array of infinitely long wires. For $n = 0$, $J_r \propto 1/r^2$, which is the general solution of Laplace's equation to the first harmonic on a sphere (P_0^1 mode) and in this context, represents a hemispherical crystal.

In addition to the assumption of axisymmetry, it can be assumed that

$$\left| \frac{\partial f}{\partial r} \right| >> \left| \frac{\partial f}{\partial z} \right| \approx 0, \tag{61}$$

or no dependencies on $\hat{z}$. As shown in the Appendix, application of continuity together with $J_\theta = 0$ invoked will then result in no radial forces, hence no radial velocity u_r which leaves the angular velocity u_θ, dependent only on r, as the dominant variable. Consequently, the Navier-Stokes equation becomes 1-dimensional in r.

For a low magnetic field $\mathbf{B_0}$, the Navier-Stokes equation is

$$\mu \left(\frac{\partial^2 u_\theta}{\partial r^2} + \frac{1}{r}\frac{\partial u_\theta}{\partial r} - \frac{u_\theta}{r^2} \right) - J_0 B_0 \left(r^{n-2} - W_p^{n-2} \right) = 0. \tag{62}$$

The particular solution of (62) takes the form of

$$u_\theta = A_1 r + A_2 r^{-1} + A_3 r^n + A_4 r^2 \tag{63}$$

where, on the right hand side, the third term accounts for the Lorentz force and the last term ensures $J_r|_{r=W_p} = 0$ is satisfied. Substituting (63) into (62) together with the following boundary conditions

$$u_\theta|_{r=r_0} = 0, \tag{64}$$

$$u_\theta|_{r=W_p} = 0 \tag{65}$$

gives

$$A_1 = \frac{J_0 B_0}{3\mu\left(n^2-1\right)\left(W_p^2 - r_0^2\right)}\left(3r_0^{n+1}\right. \\ \left. - \left(n^2-1\right) r_0^3 W_p^{n-2} + \left(n^2-4\right) W_p^{n+1}\right) \\ = \frac{J_0 B_0}{\mu} C_1, \tag{66}$$

$$A_2 = \frac{J_0 B_0}{3\mu\left(n^2-1\right)\left(W_p^2 - r_0^2\right)} r_0 \left(-3r_0^n W_p^2\right. \\ \left. + \left(n^2-1\right) r_0^2 W_p^n - r_0\left(n^2-4\right) W_p^{n+1}\right) \\ = \frac{J_0 B_0}{\mu} C_2, \tag{67}$$

$$A_3 = \frac{J_0 B_0}{\mu}\frac{1}{\left(n^2-1\right)} = \frac{J_0 B_0}{\mu} C_3, \tag{68}$$

$$A_4 = -\frac{J_0 B_0}{\mu}\frac{W_p^{n-2}}{3} = \frac{J_0 B_0}{\mu} C_4. \tag{69}$$

Note that as $|n| \to 1$, application of L'Hôpital's rule shows that the above coefficients remain finite.

Under a high magnetic field $\mathbf{B}_\infty$, the Navier-Stokes equation becomes

$$-J_r B_\infty - \sigma u_\theta B_\infty^2 = 0 \tag{70}$$

and substituting J_r from (60) gives

$$u_\theta = -\frac{J_0\left(r^{n-2} - W_p^{n-2}\right)}{\sigma B_\infty}. \tag{71}$$

A full derivation of the low and high parallel magnetic field solutions can be found in the Appendix.

The periodic boundaries for the numerical model constructed with a Cartesian grid represent cubic packing of the dendritic array but the derivation of analytic solutions was based on the assumption of axisymmetry. To asses the validity of this assumption, the following analyses compare analytic and numerical solutions determined along on-axis ($x = x$) as well as off-axis ($x = y$) sections. For off-axis comparisons, the analytic results were calculated with W_p increased by a factor of $\sqrt{2}$ to account for the increased distance between diagonal dendrite neighbours.

For a consistent comparison between results determined by the analytic and numerical solutions, the radial current density J_r as given by (60) was first fitted to the numerical results by adjusting n. Figure 9 shows the least-squares fit for a particular array of dendrites with $W_p = 18.0\mu$m which was achieved using $n = 0.96$ on-axis and $n = 0.98$ off-axis. As $W_p \to \infty$, least-squares fit of the numerical results gave $n = 0.64$ on-axis and $n = 0.72$ off-axis. These values of n lying between 0 and 1 simply reflect the dendrite morphology which is a combination of the columnar structure ($n = 1$) and hemispherical tip ($n = 0$).

The on-axis and off-axis flow profiles from the analytic and numerical solutions with $W_p = 18.0\mu$m are shown in figure 10. In the case of low magnetic field ($B_z = 10^{-7}$T), both the analytic and numerical solutions exhibit similar characteristics although the on-axis analytic solution is in better agreement with the numerical results than the off-axis solution. In contrast, the results of the high magnetic field case ($B_z = 10$T) for both on-axis and off-axis show no discernible differences between the analytic and numerical solutions except for decreasing radius $r < 4\mu$m where the analytic solutions diverge from the numerical solutions. This divergence was expected as viscous damping, which was neglected in the derivation of the analytic solutions, becomes significant.

The disparity in the match accuracy of the analytic solutions between the low and high magnetic field cases shown in figure 10 can be traced to the assumption of axisymmetry. Figure 11 shows contour plots of velocities on the tip plane extracted from the numerical results for the low and high magnetic field cases. In the high field case, axisymmetry is clearly evident whereas in the low field case, the flow pattern is affected by neighbouring dendrites. Nevertheless, the core results for the latter becomes axisymmetic for decreasing r indicating that axisymmetry remains a valid assumption for deriving analytic solutions.

The critical magnetic field is defined as before by

$$\left.\frac{\partial u_\theta}{\partial B_z}\right|_{B_z = B_c} = 0. \tag{72}$$

By applying the same procedure as described previously of equating the low magnetic field and high magnetic field solutions, the critical magnetic field can be solved as

$$B_c = \left(\frac{\mu\alpha_1}{\sigma r\alpha_2 + r_0 W_p^2 \alpha_3 + r^2\alpha_4}\right)^{\frac{1}{2}} \tag{73}$$

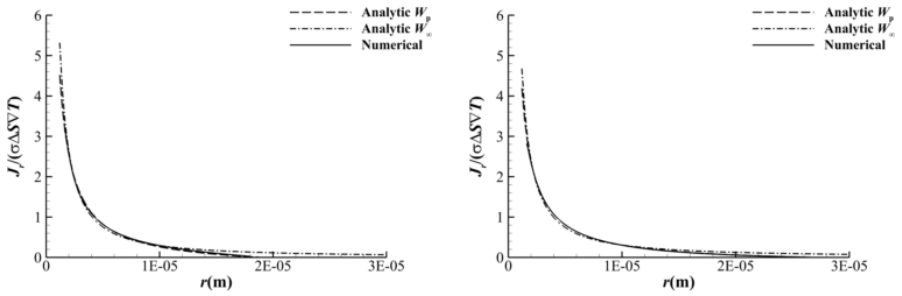

Figure 9: Numerical and analytic fits for the radial component of **J** along the axis and off axis

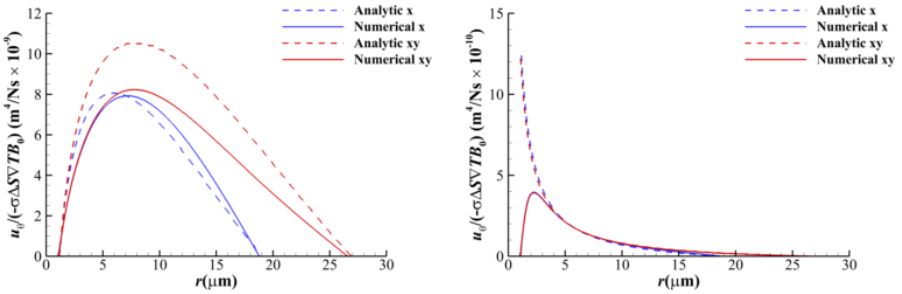

Figure 10: u_θ flow profile. Left: Low magnetic field. Right: High magnetic field.

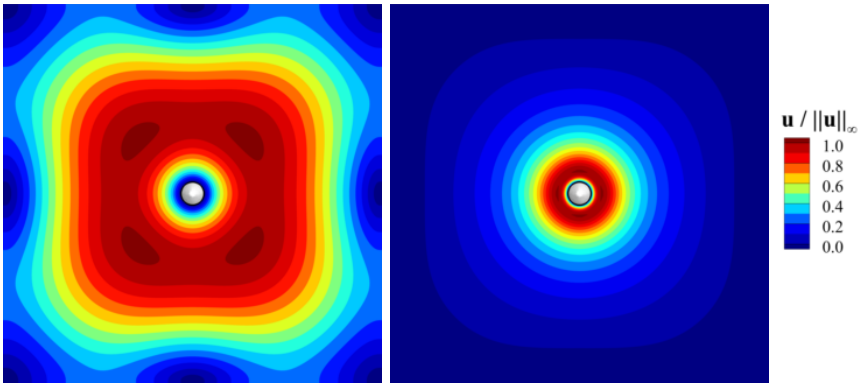

Figure 11: Velocity contours. Left: Low magnetic field. Right: High magnetic field.

where

$$\begin{aligned}
\alpha_1 &= 3\left(n^2-1\right)\left(r_0^2-W_p^2\right)\left(r^nW_p^2-r^2W_p^n\right),\\
\alpha_2 &= \left(n^2-1\right)r^3W_p^n\left(r_0^2-W_p^2\right)\\
&\quad -3r^{n+1}W_p^2\left(r_0^2-W_p^2\right),\\
\alpha_3 &= -3r_0^nW_p^2+\left(n^2-1\right)r_0^2W_p^n\\
&\quad -\left(n^2-4\right)r_0W_p^{n+1},\\
\alpha_4 &= 3r_0^{n+1}W_p^2-\left(n^2-1\right)r_0^3W_p^n\\
&\quad +\left(n^2-4\right)W_p^{n+3}.
\end{aligned}$$

The critical velocity $u_{\theta c}$ is defined as the velocity associated with the critical magnetic field at a given radius and can be solved by substituting B_c into either the high or low magnetic field solution. Using the high magnetic field solution gives

$$u_{\theta c} = -\frac{J_0\left(r^{n-2}-W_p^{n-2}\right)}{\sigma B_c}. \tag{74}$$

The critical radius r_c is defined as the radius where the critical velocity reaches its maximum or where

$$\left.\frac{\partial u_{\theta c}}{\partial r}\right|_{r=r_c} = 0 \tag{75}$$

which leads to

$$\begin{aligned}
&Q_5r_c^5+Q_4r_c^4+Q_{n+3}r_c^{n+3}+Q_{n+2}r_c^{n+2}\\
&+Q_{2n+1}r_c^{2n+1}+Q_2r_c^2+Q_nr_c^n=0
\end{aligned} \tag{76}$$

where

$$\begin{aligned}
Q_5 &= 2\left(n^2-1\right)W_p^{2n}\left(r_0^2W_p^2\right),\\
Q_4 &= W_p^n\left(3r_0^{n+1}W_p^2-\left(n^2-1\right)r_0^3W_p^n\right.\\
&\quad \left.+\left(n^2-4\right)W_p^{n+3}\right),\\
Q_{n+3} &= \left(n^3+2n\right)W_p^{n+2}\left(W_p^2-r_0^2\right),\\
Q_{n+2} &= -\left(n-1\right)W_p^2\left(3r_0^{n+1}W_p^2\right.\\
&\quad \left.-\left(n^2-1\right)r_0^3W_p^n+\left(n^2-4\right)W_p^{n+3}\right),\\
Q_{2n+1} &= 6\left(n-1\right)W_p^4\left(r_0^2-W_p^2\right),\\
Q_2 &= -r_0W_p^{n+2}\left(-3r_0^nW_p^2\right.\\
&\quad \left.+\left(n^2-1\right)r_0^2W_p^n-\left(n^2-4\right)r_0W_p^{n+1}\right),\\
Q_n &= -\left(n-3\right)r_0W_p^4\left(-3r_0^nW_p^2\right.\\
&\quad \left.+\left(n^2-1\right)r_0^2W_p^n-\left(n^2-4\right)r_0W_p^{n+1}\right).
\end{aligned}$$

A general explicit solution of (76) for r_c is not immediately evident but r_c can be determined numerically, for example, by Newton-Raphson. As an illustration, a system with $B_{cx} = 2.8$T and $B_{cxy} = 3.4$T is shown in figure 12 where the results for $u_{\theta c}$ extracted from numerical simulation of (74) are compared with the asymptotic solutions for the low and high magnetic field cases. The values of $r_{cx} = 2.4\mu$m and $r_{cxy} = 2.6\mu$m determined at the intersection of the asymptotic solutions from (76) under-estimates the simulation results indicating that the deviation of the analytic $r_c(B_c)$ from the numerical simulation is influenced more by the low field asymptotic solution than the high field solution. The low field solution also impacts the on-axis and off-axis results. Figure 13, which plots contours of velocity in the (r, B) plane, illustrates that the mismatch of the on-axis and off-axis contours become more pronounced when the decreasing magnetic field strength is coupled with increasing radius from the tip. This figure is simply an enhanced presentation of the observations regarding the assumption of axisymmetry discussed earlier and illustrated in figure 11.

For convective transport, the flow rates for both the low and high field solution can be derived by integrating u_θ between the tip radius and the primary arm spacing. The asymptotic flow rate solutions $u_{\theta fr}$ for the low and high magnetic fields are

$$\begin{aligned}
u_{\theta fr}(B_0) &= \int_{r=r_0}^{r=W_p} u_\theta dr\\
&= \frac{J_0B_0}{\mu}\left(\frac{C_1}{2}\left(W_p^2-r_0^2\right)\right.\\
&\quad +C_2\left(\ln W_p-\ln r_0\right)\\
&\quad +\frac{C_3}{n+1}\left(W_p^{n+1}-r_0^{n+1}\right)\\
&\quad \left.+\frac{C_4}{3}\left(W_p^3-r_0^3\right)\right),
\end{aligned} \tag{77}$$

$$\begin{aligned}
u_{\theta fr}(B_\infty) &= \int_{r=r_0}^{r=W_p} u_\theta dr\\
&= -\frac{J_0}{\sigma B_\infty}\left(\left(W_p^{n-1}-r_0^{n-1}\right)/\left(n-1\right)\right.\\
&\quad \left.+r_0W_p^{n-2}-W_p^{n-1}\right).
\end{aligned} \tag{78}$$

Equating (77) to (78) and setting $B_{cfr} = B_0 = B_\infty$, the critical flow rate field can be expressed as

$$B_{cfr} = \left(-\frac{\mu\alpha_1}{\sigma\left(\alpha_2+\alpha_3\right)}\right)^{\frac{1}{2}} \tag{79}$$

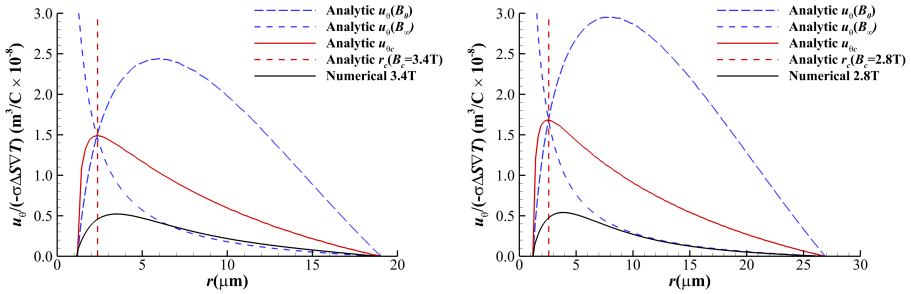

Figure 12: Asymptotic solutions, critical velocity $u_{\theta c}$ and numerical solution as a function of radius. Left: On-axis solutions with $r_c(B_c = 3.4\text{T}) = 2.4\mu\text{m}$. Right: On-axis solutions with $r_c(B_c = 2.8\text{T}) = 2.6\mu\text{m}$.

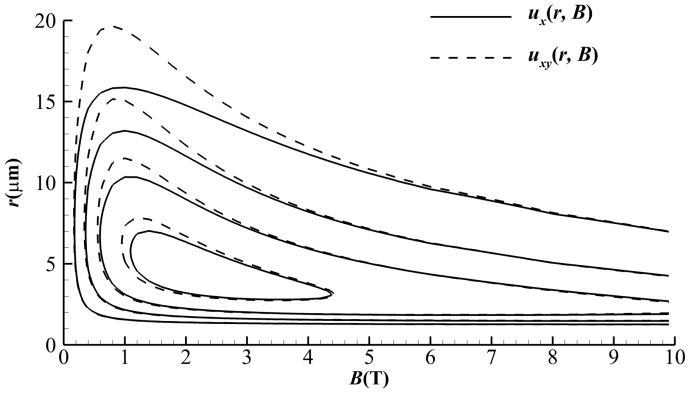

Figure 13: Contours of velocity for the on axis and off axis numerical solutions with analytic and numerical values of u_c posted.

where

$$\alpha_1 = \frac{W_p^{n-1} - r_0^{n-1}}{n-1} + r_0 W_p^{n-2} - W_p^{n-1},$$
$$\alpha_2 = \frac{C_1}{2}\left(W_p^2 - r_0^2\right) + C_2\left(\ln W_p - \ln r_0\right),$$
$$\alpha_3 = \frac{C_3}{n+1}\left(W_p^{n+1} - r_0^{n+1}\right) + \frac{C_4}{3}\left(W_p^3 - r_0^3\right).$$

Figure 14 illustrates the critical flow rate corresponding to magnetic field B_{cfr} predicted by (79) in context with the numerical solutions for determining the maximum flow rate both on-axis and off-axis. Also shown in this figure are the continuous functions $u_{\theta fr}(B)$ which link the low and high field asymptotic solutions on-axis and off-axis. The linkage has the same form as that for the transverse magnetic fields (51) but with the coefficients of F_0 and F_∞ replaced with those of B_0 and B_∞^{-1} in (77) and (78) for parallel fields. The results in figure 14 shows that (79) is an excellent predictor for the critical magnetic field as the on-axis and off-axis results for B_{cfr}, 1.8T and 1.3T, calculated using (79) are comparable to the simulation results of $B_{cfr} = 1.4$T and $B_{cfr} = 1.1$T.

The following analyses address the impact of n, W_p and r_0 on the critical magnetic field by examining the functional dependence of B_{cfr} as given by (79). The material property ratio μ/σ determines the relative magnitude of the critical magnetic field and is independent of n, W_p and r_0. Therefore, B_{cfr} is scaled by $(\mu/\sigma)^{\frac{1}{2}}$.

Figure 15 shows contours of $B_{cfr}(Wp, r_0)$ calculated from (79) for values of $n = 0$ and $n = 0.96$ which essentially cover the range of dendrite morphologies expected in most industrial applications. The B_{cfr} surfaces shown in this figure exhibit similar characteristics for both values of n indicating that B_{cfr} is not strongly dependent on n apart from lower values of $r_0 < 25\mu$m. Cross sections of B_{cfr}, as illustrated by the ones along $W_p = 200\mu$m shown in figure 16, confirm the weak dependence of B_{cfr} over the range of n considered. The dependency of B_{cfr} on r_0 as illustrated in figures 15 and 16 shows the increase of B_{cfr} from a low trough as r_0 approaches both its limits of 0 and W_p is a direct consequence of the characteristic length being dependent either on r_0 for small tips or on the difference $W_p - r_0$. In the case of $r_0 \sim W_p$, a cellular-like structure without any dendritic network will be formed as is often seen in low concentration slow solidifications.

In a manner similar to the dependency on tip radius, the dependency of the critical magnetic field on W_p is next analysed by examining cross-sections along r_0 of the $B_{cfr}(W_p, r_0)$ surfaces shown in figure 15. Figure 17, which displays cross-sections along $r_0 = 10\mu$m, not only confirms the weak dependency on n but also shows the decreasing trend of B_{cfr} to zero as $W_p \to \infty$.

The analytic solution for the critical magnetic field as $W_p \to \infty$ is of particular interest for industrial applications as it can represent, for example, a single crystal emerging from the grain selector during the casting of turbine blades. W_p would represent the distance of the dendrite to the walls of the cast where the thermal and solute boundary layers can be assumed to be much smaller than W_p with $r_0 << W_p$. By maximising the velocity instead of flow rate, a critical magnetic field for this system can be determined dependent primarily on the tip radius r_0 and the exponent n characterising the decay of the thermoelectric current J_r away from the dendrite interface as shown in the following analysis.

As $W_p \to \infty$, the low field solution for u_θ (63) becomes

$$u_\theta = \frac{J_0 B_0}{\left(n^2-1\right)\mu}\left(\frac{r^{n+1} - r_0^{n+1}}{r}\right) \tag{80}$$

and likewise the high field solution (71) becomes

$$u_\theta = -\frac{J_0 r^{n-2}}{\sigma B_\infty}. \tag{81}$$

Equating (80) to (81) and setting $B_c = B_0 = B_\infty$, the critical field can be solved as

$$B_c = \left(\frac{\mu\left(1-n^2\right)}{\sigma\left(r_c^2 - r_c^{1-n} r_0^{n+1}\right)}\right)^{\frac{1}{2}} \tag{82}$$

which on re-substituting into the high field solution (81) gives

$$u_\theta = \frac{-J_0 r_c^{n-2}}{\sigma\left(\frac{\mu(n^2-1) r_c^n}{\sigma\left(r_c r_0^{n+1} - r_c^{n+2}\right)}\right)^{\frac{1}{2}}}. \tag{83}$$

The maximum velocity occurs when

$$\frac{\partial u_\theta}{\partial r_c} = -\frac{\mu J_0 r_c^{2n}\left(\alpha_1 - \alpha_2\right)}{\sigma^2 r_c^4 \alpha_3 \alpha_4} = 0 \tag{84}$$

where

$$\alpha_1 = \left(n^3 - 3n^2 - n + 3\right) r_0^{n+1},$$
$$\alpha_2 = \left(2n^3 - 2n^2 - 2n + 2\right) r_c^{n+1},$$
$$\alpha_3 = \left(2r_0^{2n+2} - 4 r_c r_0^{n+1} + 2 r_c^{2n+2}\right),$$
$$\alpha_4 = \left(\frac{\mu\left(n^2-1\right) r_c^n}{\sigma\left(r_c r_0^{n+1} - r_c^{n+2}\right)}\right)^{\frac{3}{2}},$$

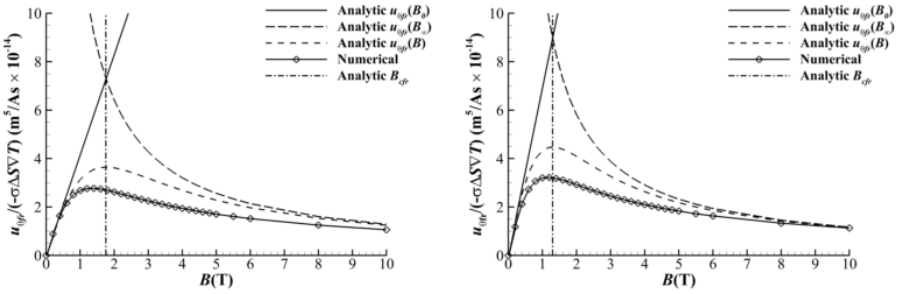

Figure 14: Flow rates from a parallel magnetic field for with indications of B_{cfr}. Left: On-axis solution. Right: Off-axis solution.

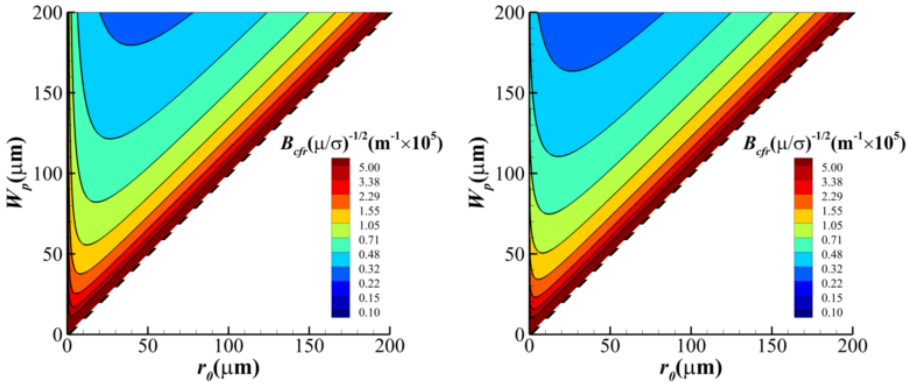

Figure 15: Contour plots of $B_{cfr}\left(W_p, r_0\right)$. Left: $n = 0$. Right: $n = 0.96$

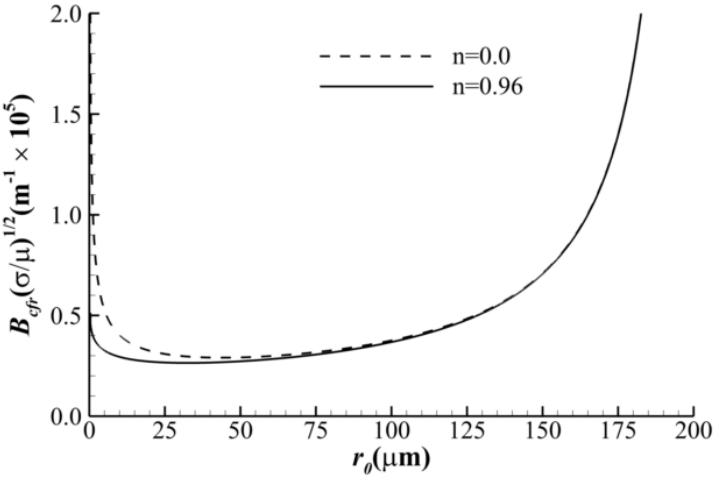

Figure 16: The functional dependence of r_0 on B_{cfr} with $W_p = 200\mu$m

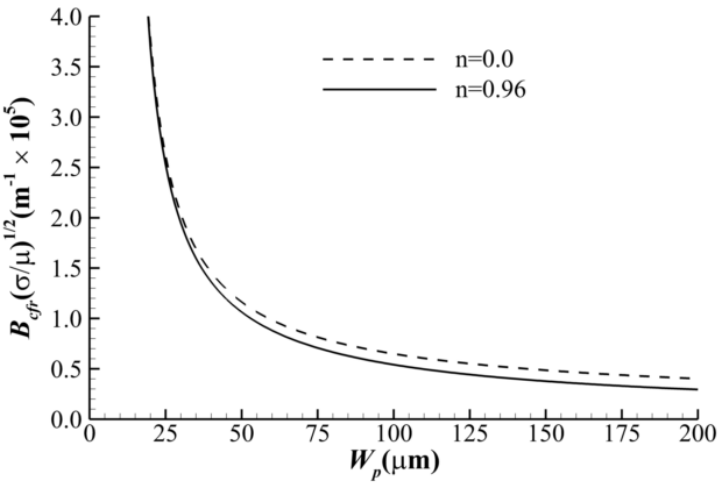

Figure 17: The functional dependence of W_p on B_{cfr} with $r_0 = 10\mu$m

which can be solved to give

$$r_c = \left(\frac{n-3}{2n-2}\right)^{\frac{1}{n+1}} r_0. \tag{85}$$

Substituting (85) into (82) gives B_c as

$$B_c = \frac{1}{r_0}\left(\frac{\mu\left(1-n^2\right)}{\sigma\left(\lambda^2-\lambda^{1-n}\right)}\right)^{\frac{1}{2}} \tag{86}$$

where

$$\lambda = \left(\frac{n-3}{2n-2}\right)^{\frac{1}{n+1}}.$$

For typical values of tip radius $r_0 = 10\mu$m and $n = 2/3$ together with material properties $\mu = 10^{-3}$Pas and $\sigma = 10^7$S/m for an aluminium-based alloy, (86) gives a critical field strength of around 0.7T which is within the range of permanent rare earth magnets.

Conclusion

The effects of an externally applied magnetic field on microscopic Thermoelectric Magnetohydroydnamics (TEMHD) during directional solidification have been explored. Analytic solutions for TEMHD with both transverse and parallel magnetic fields have been derived in the form of asymptotic solutions for low and high magnetic field intensities. By maximising the velocity and flow rate, critical magnetic fields can be determined for various solidification conditions. The magnetic field intensities predicted analytically compare well with the results computed in numerical simulations with magnitudes of field intensity consistent with those applied in current on-going experiments where significant microstructural changes have been observed. The analytic solutions show that the critical magnetic field is highly dependent on a combination of characteristic lengths of materials which include the tip radius, primary arm spacing, grain spacing and dendrite arm radius. These analytic solutions provide useful formulae that can be readily evaulated for prelimary results on critical magnetic fields in support of detailed numerical simulations as well as experimental design.

References

[1] A. Kao and K. Pericleous, "A numerical model coupling thermoelectricity, magnetohydrodynamics and dendritic growth," *Journal of Algorithms and Computational Technology*, vol. 6 No. 1, pp. 173–201, 2012.

[2] A. Kao and K. Pericleous, "The effect of secondary arm growth on thermoelectric magnetohydrodynamics," *Magnetohydrodynamics*, vol. 48 (2), pp. 361–370, 2012.

[3] A. Kao and K. Pericleous, "Investigating magnetic field orientation as an operational parameter in thermo-electric mhd solidification," *Journal of Iron and Steel International*, vol. 19 (S1-1), pp. 260–264, 2012.

[4] A. Kao, G. Djambazov, K. Pericleous, and V. Voller, "Thermoelectric mhd in dendritic solidification," *Magnetohydrodynamics*, vol. 45 (3), pp. 305–315, 2009.

[5] B. Appolaire, V. Albert, H. Combeau, and G. Lesoult, "Experimental study of free growth of equiaxed nh4cl crystals settling in undercooled nh4cl-h2o melts," *Acta Materialia*, vol. 46, Issue 16, pp. 5851–5862, 1999.

[6] A. Ramani and C. Beckermann, "Dendrite tip growth velocities of settling nh_4cl equiaxed crystals," *Scripta Materialia*, vol. 36, Issue 6, pp. 633–638, 1997.

[7] L. Tan and N. Zabaras, "A level set simulation of dendritic solidification of multicomponent alloys," *Journal of Computational Physics*, vol. 221, pp. 9–40, 2007.

[8] N. Al-Rawahi and G. Tryggvason, "Numerical simulation of dendritic solidification with convection: Three-dimensional flow," *Journal of Computational Physics*, vol. 194, pp. 677–696, 2004.

[9] J. A. Shercliff, "Thermoelectric magnetohydrodynamics," *Journal of Fluid Mechanics*, vol. 91, part 2, pp. 231–251, 1978.

[10] J. A. Shercliff, "The pipe end problem in thermoelectric mhd," *Journal of Applied Mathematics and Physics*, vol. 31, pp. 94–112, 1980.

[11] J. A. Shercliff, "Thermoelectric mhd with walls parallel to the magnetic field," *International Journal of Heat and Mass Transfer*, vol. 23, pp. 1219–1228, 1980.

[12] M. A. Jaworski, T. K. Gray, M. Antonelli, J. J. Kim, C. Y. Lau, M. B. Lee, M. J. Neumann, W. Xu, and D. N. Ruzic, "Thermoelectric magnetohydrodynamic stirring of liquid metals," *Physical Review Letters*, vol. 104, p. 094503, 2010.

[13] X. Zhang, A. Cramer, A. Lange, and G. Gerbeth, "Model experiments on macroscopic thermoelectromagnetic convection," *Magnetohydrodynamics*, vol. 45, pp. 25–42, 2009.

[14] A. Cramer, X. Zhang, and G. Gerbeth, "Macroscopic thermomagnetic convection: a more generic case and optimization," *Magnetohydrodynamics*, vol. 45, pp. 505–510, 2009.

[15] M. Kaneda, T. Tagawa, and H. Ozoe, "Natural convection of liquid metal in a cube with seebeck effect under a magnetic field," *Int. J. Transport Phenomena*, vol. 4 No. 3, pp. 181–191, 2002.

[16] R. Moreau, O. Laskar, M. Tanaka, and D. Camel, "Thermoelectric magnetohydrodynamic effects on solidification of metallic alloys in the dendritic regime," *Materials Science and Engineering: A*, vol. 173, Issues 1-2, pp. 93–100, 1993.

[17] R. Moreau, O. Laskar, and M. Tanaka, "Thermoelectric and magnetohydrodynamic effects on solidifying alloys," *Magnetohydrodynamics*, vol. 32, pp. 173–177, 1996.

[18] P. Lehmann, R. Moreau, D. Camel, and R. Bolcat, "Modification of interdendritic convection in directional solidifcation by a uniform magnetic field," *Acta Materialia*, vol. 46, No. 11, pp. 4067–4079, 1998.

[19] J. Wang, Z. Ren, Y. Fautrelle, X. Li, H. Nguyen-Thi, N. Mangelinck-Noel, G. S. A. Jaoude, Y. Zhong, I. Kaldre, and A. Bojarevics, "Modification of liquid/solid interface shape in directionally solidifying alcu alloys by a transverse magnetic field," *Journal of Materials Science*, vol. 48-1, pp. 213–219, 2013.

[20] I. Kaldre, Y. Fautrelle, J. Etay, A. Bojarevics, and L. Buligins, "Thermoelectric current and magnetic field interaction influence on the structure of directionally solidified sn10 wt.% pb alloy," *Journal of Alloys and Compounds*, vol. 571, pp. 50–55, 2013.

[21] X. Li, Z. Ren, A. Gagnoud, O. Budebkova, and Y. Fautrelle, "Effects of thermoelectric magnetic convection on the solidification structure during directional solidification under lower transverse magnetic field," *Metallurgical and Materials Transactions A*, vol. 42-11, pp. 3459–3471, 2011.

[22] X. Li, A. Gagnoud, Z. Ren, Y. Fautrelle, and R. Moreau, "Investigation of thermoelectric magnetic convection and its effect on solidification structure during directional solidification under a low axial magnetic field," *Acta Materialia*, vol. 57, pp. 2180–2197, 2009.

[23] X. Li, A. Gagnoud, Y. Fautrelle, Z. Ren, and R. Moreau, "Influence of thermoelectric effects

on the morphology of alsi eutectic during directional solidification under an axial strong magnetic field," *Journal of Crystal Growth*, vol. 367, pp. 94–103, 2013.

[24] X. Li, Y. Fautrelle, K. Zaidat, A. Gagnoud, Z. Ren, R. Moreau, Y. Zhang, and C. Esling, "Columnar-to-equiaxed transitions in al-based alloys during directional solidification under a high magnetic field," *Journal of Crystal Growth*, vol. 312, pp. 267–272, 2010.

[25] X. Li, Y. Fautrelle, and Z. Ren, "Influence of thermoelectric effects on the solid-liquid interface shape and cellular morphology in the mushy zone during the directional solidification of al-cu alloys under a magnetic field," *Acta Materialia*, vol. 55, pp. 3803–3813, 2007.

[26] H. Yasuda, K. Nogita, C. Gourlay, M. Yoshiya, and T. Nagira, "In-situ observation of sn alloy solidification at spring8," *Journal of the Japan Welding Society*, vol. 78, pp. 6–9, 2009.

Appendix

Derivation of Transverse Magnetic Field Solutions

Under a transverse field, the thermoelectric force is

$$\mathbf{J}\times\mathbf{B}=\begin{vmatrix}\hat{x}&\hat{y}&\hat{z}\\0&0&J_z\\0&B_y&0\end{vmatrix}=-J_zB_y\hat{x}. \tag{87}$$

Transverse low field solution For a low magnetic field $\mathbf{B_0}$, the Navier-Stokes equation reduces to

$$-J_zB_0+\mu\frac{\partial^2u}{\partial y^2}-\frac{\partial p}{\partial x}=0. \tag{88}$$

The boundary conditions for the secondary duct are

$$u_1\big|_{y=W_s}=0, \tag{89}$$

$$\left.\frac{\partial u_1}{\partial y}\right|_{y=0}=0, \tag{90}$$

$$\left.\frac{\partial}{\partial y}\frac{\partial p_1}{\partial x}\right|_{y=0}=0 \tag{91}$$

and in the primary duct

$$u_2\big|_{y=W_p}=u_w, \tag{92}$$

$$\left.\frac{\partial u_2}{\partial y}\right|_{y=0}=0, \tag{93}$$

$$\left.\frac{\partial u_2}{\partial y}\right|_{y=W_p}=0, \tag{94}$$

$$\left.\frac{\partial}{\partial y}\frac{\partial p_2}{\partial x}\right|_{y=0}=0, \tag{95}$$

$$\left.\frac{\partial}{\partial y}\frac{\partial p_2}{\partial x}\right|_{y=W_p}=0 \tag{96}$$

where u_w is the velocity at the symmetry boundary. Conservation of mass is given by

$$\int_{y=0}^{y=W_s}u_1dy=\int_{y=0}^{y=W_p}u_2dy. \tag{97}$$

Pressure is continuous along the centre of each duct but is constrained by the periodic boundary conditions which requires negative and positive gradients for the secondary and primary ducts respectively. Assuming constant gradients within each duct, the continuity and periodic conditions for pressure can be expressed as

$$\left.\frac{\partial p_1}{\partial x}\right|_{y=0}W_r+\left.\frac{\partial p_2}{\partial x}\right|_{y=0}(W_p-W_r)=0. \tag{98}$$

The general solutions for pressure and velocity at these two points are

$$u_1=\sum_{n=0}^{\infty}A_ny^n, \tag{99}$$

$$\frac{\partial p_1}{\partial x}=\sum_{n=0}^{\infty}C_ny^n, \tag{100}$$

$$u_2=\sum_{n=0}^{\infty}D_ny^n, \tag{101}$$

$$\frac{\partial p_2}{\partial x}=\sum_{n=0}^{\infty}E_ny^n. \tag{102}$$

In view of the symmetry about the plane at $y=0$, only even integers of n are relevant. The minimum n required to represent the flow profile is determined by the number of critical points imposed by the boundary conditions. For the secondary duct, $n=2$ which represents parabolic flow. Dimensional analysis of (88) shows that (99) and (100) simplify to Poiseuille

flow.

$$u_1 = A_0 + A_2 y^2, \tag{103}$$

$$\frac{\partial p_1}{\partial x} = C_0. \tag{104}$$

In the primary duct, the symmetry conditions in (94) and (96) at $y = W_p$ imply that there are least three critical points for both the pressure gradient and velocity. Using the pressure gradient as the constraint for minimum n, (101) and (102) reduce to

$$u_2 = D_0 + D_2 y^2 + D_4 y^4 + D_6 y^6, \tag{105}$$

$$\frac{\partial p_2}{\partial x} = E_0 + E_2 y^2 + E_4 y^4. \tag{106}$$

Substituting these solutions into (88) gives

$$2\mu A_2 - C_0 = J_z B_0, \tag{107}$$

$$2\mu D_2 - E_0 = J_z B_0, \tag{108}$$

$$y^2 \left(12\mu D_4 - E_2\right) = 0, \tag{109}$$

$$y^4 \left(30\mu D_6 - E_4\right) = 0. \tag{110}$$

Continuity becomes

$$A_0 W_s + \frac{1}{3} A_2 W_s^3 - D_0 W_p - \frac{1}{3} D_2 W_p^3 - \frac{1}{5} D_4 W_p^5 - \frac{1}{7} D_6 W_p^7 = 0. \tag{111}$$

The boundary conditions from (89), (92), (94) and (96) give

$$A_0 + A_2 W_s^2 = 0, \tag{112}$$

$$D_0 + D_2 W_p^2 + D_4 W_p^4 + D_6 W_p^6 = 0, \tag{113}$$

$$2D_2 W_p + 4D_4 W_p^3 + 6D_6 W_p^5 = 0, \tag{114}$$

$$2E_2 W_p + 4E_4 W_p^3 = 0. \tag{115}$$

The periodic pressure condition (98) gives

$$C_0 W_r + E_0 \left(W_p - W_r\right) = 0. \tag{116}$$

Solving the above system of equations gives

$$A_0 = \frac{1}{2\mu W_0} \left(-16 J_z B_0 W_p^3 + 147 \mu u_w \left(W_p - W_r\right)\right) W_p W_s^2, \tag{117}$$

$$A_2 = \frac{1}{2\mu W_0} \left(16 J_z B_0 W_p^3 - 147 \mu u_w \left(W_p - W_r\right)\right) W_p, \tag{118}$$

$$C_0 = \frac{1}{W_0} \left(J_z B_0 \left(16 W_p^3 - 49 W_s^3\right) - 147 \mu u_w W_p\right) \left(W_p - W_r\right), \tag{119}$$

$$D_0 = -\frac{1}{2\mu W_0} \left(21 J_z B_0 W_s^3 W_p^3 + \mu u_w \left(31 W_p^3 W_r - 98 W_p W_s^3 + 98 W_r W_s^3\right)\right), \tag{120}$$

$$D_2 = \frac{49 J_z B_0 W_s^3 W_p + 147 \mu u_w W_p W_r}{2\mu W_0}, \tag{121}$$

$$D_4 = -\frac{35 J_z B_0 W_s^3 + 105 \mu u_w W_r}{2\mu W_p W_0}, \tag{122}$$

$$D_6 = \frac{7 J_z B_0 W_s^3 + 21 \mu u_w W_r}{2\mu W_p^3 W_0}, \tag{123}$$

$$E_0 = \frac{1}{W_0} \left(J_z B_0 \left(-16 W_p^3 + 49 W_s^3\right) + 147 \mu u_w W_p\right) W_r, \tag{124}$$

$$E_2 = -\frac{210 J_z B_0 W_s^3 + 630 \mu u_w W_r}{W_p W_0}, \tag{125}$$

$$E_4 = \frac{105 J_z B_0 W_s^3 + 315 \mu u_w W_r}{W_p^3 W_0} \tag{126}$$

where

$$W_0 = 49 W_s^3 \left(W_p - W_r\right) + 16 W_p^3 W_r. \tag{127}$$

Transverse high field solution For a high magnetic field $\mathbf{B}_\infty$, the damping term reduces to

$$\sigma \mathbf{u} \times \mathbf{B} = \sigma \begin{vmatrix} \hat{x} & \hat{y} & \hat{z} \\ u_x & 0 & 0 \\ 0 & B_y & 0 \end{vmatrix} = \sigma u_x B_y \hat{z}, \tag{128}$$

$$\sigma \mathbf{u} \times \mathbf{B} \times \mathbf{B} = \sigma \begin{vmatrix} \hat{x} & \hat{y} & \hat{z} \\ 0 & 0 & u_x B_y \\ 0 & B_y & 0 \end{vmatrix} = -\sigma u_x B_y^2 \hat{x}. \tag{129}$$

The Navier-Stokes equation at x_1 and x_2 becomes respectively

$$-J_z B_\infty - \sigma u_1 B_\infty^2 - \frac{\partial p_1}{\partial x} = 0, \tag{130}$$

$$-J_z B_\infty - \sigma u_2 B_\infty^2 - \frac{\partial p_2}{\partial x} = 0. \tag{131}$$

Periodic pressure condition gives

$$\frac{\partial p_1}{\partial x} W_r + \frac{\partial p_2}{\partial x} (W_p - W_r) = 0 \tag{132}$$

and continuity

$$\int_{y=0}^{y=W_s} u_1 dy = \int_{y=0}^{y=W_p} u_2 dy \tag{133}$$

reduces to

$$u_1 = u_2 \frac{W_p}{W_s}. \tag{134}$$

Solving gives

$$u_1 = -\frac{J_z W_p^2}{\sigma B_\infty W_\infty}, \tag{135}$$

$$u_2 = -\frac{J_z W_p W_s}{\sigma B_\infty W_\infty}, \tag{136}$$

$$\frac{\partial p_1}{\partial x} = \frac{J_z B_\infty (W_r - W_p)(W_p - W_s)}{W_\infty}, \tag{137}$$

$$\frac{\partial p_2}{\partial x} = -\frac{J_z B_\infty W_r (W_p - W_s)}{W_\infty}, \tag{138}$$

$$W_\infty = W_r (W_p - W_s) + W_p W_s. \tag{139}$$

Derivation of Parallel Magnetic Field Solutions

The Lorentz force for a parrellel magnetic field in is given by

$$\mathbf{J} \times \mathbf{B_z} = \begin{vmatrix} \hat{r} & \hat{\theta} & \hat{z} \\ J_r & J_\theta & J_z \\ 0 & 0 & B_z \end{vmatrix} = J_\theta B_z \hat{r}, -J_r B_z \hat{\theta} \tag{140}$$

where J_r is assumed to take a power law in the form of

$$J_r = J_0 \left(r^{n-2} - W_p^{n-2} \right). \tag{141}$$

The problem is assumed to be axisymmetric, hence

$$\frac{\partial \Psi}{\partial \theta} = \frac{\partial u_\theta}{\partial \theta} = \frac{\partial p}{\partial \theta} = 0. \tag{142}$$

It is also assumed that

$$\left| \frac{\partial u_\theta}{\partial r} \right| >> \left| \frac{\partial u_\theta}{\partial z} \right| \approx 0, \tag{143}$$

$$\left| \frac{\partial p}{\partial r} \right| >> \left| \frac{\partial p}{\partial z} \right| \approx 0, \tag{144}$$

hence there are no dependencies on $\hat{z}$. From (142), $J_\theta = 0$. The Lorentz force therefore only has component in $\hat{\theta}$. For axisymmetry with no dependency on $\hat{z}$, the continuity equation

$$\nabla \cdot \mathbf{u} = \frac{1}{r} \frac{\partial r u_r}{\partial r} + \frac{1}{r} \frac{\partial u_\theta}{\partial \theta} + \frac{\partial u_z}{\partial z} = 0. \tag{145}$$

becomes

$$\nabla \cdot \mathbf{u} = \frac{1}{r} \frac{\partial r u_r}{\partial r} = 0 \tag{146}$$

which can be solved as

$$u_r = \frac{C}{r} \tag{147}$$

where C is the constant of integration. Applying the boundary condition

$$u_r|_{r=r_0} = 0, \tag{148}$$

$C = 0$ hence $u_r = 0$ for all r.

Parallel low field solution For a low magnetic field $\mathbf{B_0}$, the Navier-Stokes equation becomes

$$-\nabla p + \mu \nabla^2 \mathbf{u} + \mathbf{J} \times \mathbf{B_0} = 0. \tag{149}$$

For a low Re,

$$\frac{\mathbf{u}}{r^2} \propto \nabla^2 \mathbf{u} \tag{150}$$

implying

$$\mathbf{u} \propto \nabla p + \mathbf{J} \times \mathbf{B_0}. \tag{151}$$

Therefore with no radial velocity or radial Lorentz force

$$\left(\nabla^2 \mathbf{u} \right) \cdot \hat{r} = \frac{\partial p}{\partial r} = 0 \tag{152}$$

the problem reduces to a 1-dimensional force balance in $\hat{\theta}$

$$\mu \left(\frac{\partial^2 u_\theta}{\partial r^2} + \frac{1}{r} \frac{\partial u_\theta}{\partial r} - \frac{u_\theta}{r^2} \right) - J_0 B_0 \left(r^{n-2} - W_p^{n-2} \right) = 0. \tag{153}$$

The general solution of

$$\mu \left(\frac{\partial^2 u_\theta}{\partial r^2} + \frac{1}{r} \frac{\partial u_\theta}{\partial r} - \frac{u_\theta}{r^2} \right) = 0 \tag{154}$$

is

$$u_\theta = A_1 r + A_2 r^{-1}. \tag{155}$$

However, to account for the extra force in (153), two additional terms were appended to give a particular solution taking the form of

$$u_\theta = A_1 r + A_2 r^{-1} + A_3 r^n + A_4 r^2 \tag{156}$$

where, on the right hand side, the third term accounts for the Lorentz force and the last term ensures the boundary condition of $J_r|_{r=W_p} = 0$ is satisfied. Substituting into (153) gives

$$\begin{aligned}\left(\mu\left(n^2-1\right)A_3 r^{n-2} - J_0 B_0 r^{n-2}\right)&\\ +\left(3\mu A_4 + J_0 B_0 W_p^{n-2}\right) = 0,& \quad (157)\\ \mu\left(n^2-1\right)A_3 r^{n-2} - J_0 B_0 r^{n-2} = 0,& \quad (158)\\ \left(3\mu A_4 + J_0 B_0 W_p^{n-2}\right) = 0.& \quad (159)\end{aligned}$$

Applying the boundary conditions

$$\begin{aligned}u_\theta|_{r=r_0} = 0,& \quad (160)\\ u_\theta|_{r=W_p} = 0& \quad (161)\end{aligned}$$

gives

$$\begin{aligned}A_1 r_0 + A_2 r_0^{-1} + A_3 r_0^n + A_4 r_0^2 = 0,& \quad (162)\\ A_1 W_p + A_2 W_p^{-1} + A_3 W_p^n + A_4 W_p^2 = 0.& \quad (163)\end{aligned}$$

Solving the above system of equations gives

$$\begin{aligned}A_1 =& \frac{J_0 B_0}{3\mu\left(n^2-1\right)\left(W_p^2 - r_0^2\right)}\left(3r_0^{n+1}\right.\\ &-\left.\left(n^2-1\right)r_0^3 W_p^{n-2} + \left(n^2-4\right)W_p^{n+1}\right)\\ &= \frac{J_0 B_0}{\mu}C_1, \quad (164)\\ A_2 =& \frac{J_0 B_0}{3\mu\left(n^2-1\right)\left(W_p^2 - r_0^2\right)} r_0\left(-3r_0^n W_p^2\right.\\ &+\left.\left(n^2-1\right)r_0^2 W_p^n - r_0\left(n^2-4\right)W_p^{n+1}\right)\\ &= \frac{J_0 B_0}{\mu}C_2, \quad (165)\\ A_3 =& \frac{J_0 B_0}{\mu}\frac{1}{\left(n^2-1\right)} = \frac{J_0 B_0}{\mu}C_3, \quad (166)\\ A_4 =& -\frac{J_0 B_0}{\mu}\frac{W_p^{n-2}}{3} = \frac{J_0 B_0}{\mu}C_4. \quad (167)\end{aligned}$$

Application of L'Hôpital's rule as $n \to -1$

$$\begin{aligned}u_\theta =& A_1 r + \left(A_2 + A_3\right)r^{-1} + A_4 r^2, \quad (168)\\ \lim_{n\to-1}\left(A_2 + A_3\right) =& -B_0 J_0\left(3W_p^3 \ln r_0 + r_0^2\right.\\ &\left.\left(2r_0 - 2W_p - 3W_p \ln W_p\right)\right)/\\ &6\mu W_p\left(r_0^2 - W_p^2\right), \quad (169)\\ \lim_{n\to-1} A_1 =& B_0 J_0\left(2r_0^3 - 2W_p^3 -\right.\\ &\left.3r_0^2 W_p \ln r_0 + 3W_p^3 \ln W_p\right)/\\ &6\mu\left(r_0^2 W_p - W_p^3\right) \quad (170)\end{aligned}$$

and as $n \to 1$

$$\begin{aligned}u_\theta =& \left(A_1 + A_3\right)r + A_2 r^{-1} + A_4 r^2, \quad (171)\\ \lim_{n\to1}\left(A_1 + A_3\right) =& B_0 J_0\left(2r_0^3 - 2W_p^3 -\right.\\ &\left.3r_0^2 W_p \ln r + 3W_p^3 \ln W_p\right)/\\ &6\mu\left(r_0^2 W_p - W_p^3\right), \quad (172)\\ \lim_{n\to1} A_2 =& -B_0 J_0 r_0^2 W_p\left(2r_0 - W_p\right.\\ &\left.\left(-2 - 3\ln r_0 + 3\ln W_p\right)\right)/\\ &\left(6\mu\left(r_0^2 - W_p^2\right)\right) \quad (173)\end{aligned}$$

shows that the velocity remains finite as $|n| \to 1$.

Parallel high field solution For a high magnetic field $\mathbf{B}_\infty$, Navier-Stokes equation becomes

$$-\nabla p + \mathbf{J}\times\mathbf{B}_\infty + \mathbf{u}\times\mathbf{B}_\infty\times\mathbf{B}_\infty = 0. \quad (174)$$

With no radial velocity or radial Lorentz force

$$\mathbf{u}\times\mathbf{B}_\infty\times\mathbf{B}_{\infty r} = \mathbf{J}\times\mathbf{B}_{\infty r} = \frac{\partial p}{\partial r} = 0 \quad (175)$$

and (174) reduces to a force balance in $\hat{\theta}$

$$-J_r B_\infty - \sigma u_\theta B_\infty^2 = 0. \quad (176)$$

Substituting J_r from (141) gives

$$u_\theta = -\frac{J_0\left(r^{n-2} - W_p^{n-2}\right)}{\sigma B_\infty}. \quad (177)$$